

# Model-based Personalized Synthetic Magnetic Resonance Imaging

Subrata Pal and Ranjan Maitra and Somak Dutta

Synthetic Magnetic Resonance (MR) imaging predicts images at new design parameter settings from a few observed MR scans. Model-based methods, that use both the physical and statistical properties underlying the MR signal and its acquisition, can predict images at any setting from as few as three scans, allowing it to be used in individualized patient- and anatomy-specific contexts. However, the estimation problem in model-based synthetic MR imaging is ill-posed and so regularization, in the form of correlated Gaussian Markov Random Fields, is imposed on the voxel-wise spin-lattice relaxation time, spin-spin relaxation time and the proton density underlying the MR image. We develop theoretically sound but computationally practical matrix-free estimation methods for synthetic MR imaging. Our evaluations demonstrate excellent ability of our methods to synthesize MR images in a clinical framework and also estimation and prediction accuracy and consistency. An added strength of our model-based approach, also developed and illustrated here, is the accurate estimation of standard errors of regional means in the synthesized images.

## Index Terms

Alternating Expectation-Conditional Maximization algorithm, Bloch transform, conjugate gradient, Lanczos algorithm, multi-layered Gaussian Markov Random Field, profile likelihood, variance estimation.

## I. INTRODUCTION

Magnetic Resonance (MR) Imaging (MRI) [1]–[3] is a popular radiologic tool for visualizing tissue structure or for characterising cerebral and other functions. In MR imaging, each tissue type has a distinctive spin-lattice or longitudinal relaxation time ( $T_1$ ), spin-spin or transverse relaxation time ( $T_2$ ), and proton density ( $\rho$ ). These quantities are observed only indirectly through noise-contaminated measurements of their transformations that modulate their effect through user-controlled design parameters such as echo time (TE), repetition time (TR) or flip angle ( $\alpha$ ). Even when such images can be directly obtained, they are practically unusable owing to their low resolution [4] or acquisition times [5].

There are many ways [6]–[8] in which  $\rho$ ,  $T_1$  and  $T_2$  combine with the design parameters to form an MR image. In the specific illustrative case of spin-echo MRI used in this paper, the noiseless MR intensity ( $\nu_{ij}$ ) (assuming perfect excitation) at the  $i$ th voxel and for the  $j$ th design parameter setting of TE and TR (*i.e.* with  $(TE_j, TR_j)$ ) is approximately specified by the Bloch equation

$$\nu_{ij} = \rho_i \exp\left(-\frac{TE_j}{T_{2i}}\right) \left\{1 - \exp\left(-\frac{TR_j}{T_{1i}}\right)\right\}. \quad (1)$$

[9] predicate (1) under the simplifying assumptions of a single perfect  $\alpha = 90^\circ$  relaxation pulse followed by a recovery time of length  $TR_j$  and a delay of time  $TE_j$  for acquisition, and that  $\nu_{ij}$  is determined entirely by  $\rho_i$ ,  $T_{1,i}$  and  $T_{2,i}$  and is affected negligibly by other contrasts. In reality, of course, the observed MR signal is noise-contaminated and complex-valued because it is acquired after Fourier reconstruction on a Cartesian grid in  $K$ -space. The magnitude ( $r_{ij}$ , at the  $i$ th voxel and  $j$ th design parameter setting) of this complex-valued signal is commonly used, and is well-modeled [10]–[12] by a Rice distribution [13], [14] with density

$$\varrho(r_{ij}; \sigma_j, \nu_{ij}) = \frac{r_{ij}}{\sigma_j^2} \exp\left(-\frac{r_{ij}^2 + \nu_{ij}^2}{2\sigma_j^2}\right) \mathbb{I}_0\left(\frac{r_{ij}\nu_{ij}}{\sigma_j^2}\right), \quad (2)$$

for  $r_{ij} > 0$ . Here  $\sigma > 0$  is the scale parameter of the Rice density and  $\mathbb{I}_k(\cdot)$  is the modified Bessel function of the first kind of order  $k$ . The Rice distribution of  $r_{ij}$  follows from the approximate distribution [15] of the complex-valued MR signal as bivariate Gaussian with mean  $(\nu_{ij} \cos \eta, \nu_{ij} \sin \eta)$  and homogeneous diagonal dispersion matrix  $\sigma^2 \mathbf{I}_2$ , for some  $\eta$ . For identifiability and convenience, we use  $\eta = 0$  [9], [16], [17].

For a spin-echo MR imaging sequence [18], [19], different (TE, TR) values modulate  $T_1$ ,  $T_2$  and  $\rho$  and can be used to enhance the clinical distinction between tissues. However, the optimal (TE, TR)-settings are patient- and/or anatomy-specific and not always possible to specify in advance. Patient discomfort, such as with children or claustrophobic subjects, may, for example, preclude obtaining images with long acquisition times. This phenomenon is by no means limited to the spin-echo technique: for instance, it is not possible to gather  $T_1$  or  $T_2$  images using spoiled gradient recalled-echo (SPGR) or fully balanced steady-state free precession (SSFP) techniques, respectively [4]. Nevertheless,  $T_1$  and  $T_2$  images can, for instance, help distinguish neurologically diseased brains [20]–[25] and so may be important to acquire.

*Synthetic MRI* was proposed [26]–[30] to address the above shortcomings. In traditional synthetic MRI, the objective is to first estimate the underlying  $\rho$ ,  $T_1$ , and  $T_2$  values at a voxel from a set of *training* images and to insert these estimates along with unobserved design parameters into (1), in spin-echo MRI, to obtain corresponding synthetic images. The technique is an appealing alternative in scenarios where images at multiple settings are required, such as in pediatric imaging of the developing brain or non-cooperating subjects [31]–[33], or in patients with multiple sclerosis [34] and so on. In such situations, images with longer acquisition times can potentially be synthesized from those collected with shorter acquisition times. Another benefit is a potential reduction in motion artifacts, or the possibility of consistent image comparisons between different settings. However, despite its vast potential, synthetic MRI’s clinical adaptation has been stymied by the inherent ill-posedness of the inversion of the Bloch equation. Because a handful of training images are typically acquired, the standard voxel-wise least squares (LS) estimates of  $(\rho, T_1, T_2)$  are unstable [9], leading to the need for spatial regularization of these estimates. Bayesian solutions [35], [36] imposed a multi-layer extension of the Geman-McClure Markov random field prior [37] on  $(\rho, T_1, T_2)$ . However, instead of the Rice distribution (2), they assumed  $r_{ij}$  to be independent Gaussian with mean  $\nu_{ij}$  and variance  $\sigma_j^2$ . In order to tackle the resulting intractability of the posterior distributions, [35] resorted to a farrago of pseudo-likelihood, expectation-maximisation (EM) and Gibbs sampling while [36] used computationally intensive MCMC methods – both of which are impractical to use on three-dimensional (3D) images in a clinical setting.

An alternative approach to synthetic MRI was proposed by [9] who assumed more accurate Rice distributions (2) for the  $r_{ij}$ ’s and Gaussian Markov Random field (GMRF) structure on transformations of  $(\rho, T_1, T_2)$ . Although they correctly anticipated that such a formulation of the synthetic MRI problem should facilitate practically fast statistical computations, their estimating algorithm, the one-step late EM (OSL-EM) algorithm of [38], is not guaranteed to converge, and can provide suboptimal estimates when stricter convergence criteria are applied than in their paper.

A machine learning approach [39] using conditional generative adversarial networks (cGAN) [40] argued that  $T_1$  and  $T_2$ -weighted images, generated by the LS-based SyMRI software [41] are of good quality, but that the same can not be said of synthetically-generated FLAIR images. So they used a pixel-wise neural network approach (implemented in two-dimensions) within cGAN to improve synthetic MRI, especially for FLAIR-type images. Separately, [42] used spatial generative adversarial networks on training sets of  $T_1$ - and  $T_2$ -weighted images to predict  $T_1$  from  $T_2$  images and vice-versa. However, this approach requires both  $T_1$ - and  $T_2$ -weighted training images and is inapplicable for MRI techniques (*e.g.*, SPGR or SSFP) that can not acquire them both. In general, machine learning approaches do not work well when the settings for the acquired scans are not in the training set. The full potential for synthetic MRI in a clinical setting can be realized when we are able to acquire individualized training set images and predict synthetic images based on context and at any desired patient- or anatomy-specific settings, and not based on some database that is an input in a machine learning model. For example, it may be more optimal to choose different design parameter settings when acquiring training images for pediatric or non-cooperating patients. Further, the individual noise characteristics of a particular MRI scanner are not accounted for in a machine learning model. These issues are obviated in model-based synthetic MRI which uses the physical and statistical noise properties of the individually acquired MRI scans to synthesize additional images at any desired design parameter settings. So here, we provide new methods for more accurately and efficiently implementing the framework of [9].

The rest of our paper is as follows. Section II develops a scalable alternating expectation conditional maximization (AECM) algorithm [43] for synthetic MRI that is guaranteed to converge and essentially matches the speed of non-regularized methods such as LS. The key ingredients of our AECM algorithm are a checkerboard coloring scheme [44], [45] that allows fast parallel block maximization over the voxel-wise parameters and analytically profiles out some of the GMRF parameters, reducing the optimization over the remaining parameters to one in at most two variables. An additional appealing aspect of our model-based approach is the conceptual ease of obtaining standard error (SE) estimates of our predictions, so we provide methods for their fast implementation over specified regions. Section III evaluates properties of our estimates, and demonstrates our methodology on a normal subject in a clinical setting. We also investigate the selection of test sets for optimizing predictive performance and demonstrate consistency of our synthetic MRI predictions. A separate set of simulation experiments evaluates estimation and prediction accuracy and consistency for different noise levels. We conclude with some discussion. An online supplement with sections, figures and tables prefixed by “S”, is available. Our algorithm is implemented in a C++ library *symr* (pronounced *sim-mer*) with Matlab and R [46] wrappers and uses openMP-based parallelization for computing practicality.

## II. METHODOLOGY

### A. A penalized likelihood model for MRI

Following [9], we assume that the observed image intensities are given by  $R = \{r_{ij}\}$ , with  $r_{ij}$ s independent Rice-distributed random variables with density (2). We get the log-likelihood

$$\ell(\{T_{1i}, T_{2i}, \rho_i\}_{i=1}^n; R) = \sum_{i=1}^n \sum_{j=1}^m \log \varrho(r_{ij}; \nu_{ij}, \sigma_j), \quad (3)$$

where the voxels  $i = 1, 2, \dots, n$  are embedded in a regular  $n_x \times n_y \times n_z$  3D array. The noise parameter  $\sigma_j^2$  in each training image is estimated using [17]. As in [9], we spatially regularize  $(\rho, T_1, T_2)$  by the voxel-wise transformations  $W_{i1} = \rho_i$ ,  $W_{i2} = \exp(-1/T_{1i})$ , and  $W_{i3} = \exp(-1/T_{2i})$  and penalizing (3) to obtain the optimization problem

$$\max_{\mathbf{W}} \left\{ \ell(\mathbf{W}; R) - \frac{1}{2} \text{Tr} \Psi^{-1} \mathbf{W}' \Lambda \mathbf{W} \right\}. \quad (4)$$

In (4),  $\mathbf{W} = (W_{ik})$  is a  $n \times 3$  matrix,  $\Psi$  is a  $3 \times 3$  positive definite matrix and  $\Lambda = \beta_z \mathbf{J}_{n_z} \otimes \mathbf{I}_{n_y} \otimes \mathbf{I}_{n_x} + \beta_y \mathbf{I}_{n_z} \otimes \mathbf{J}_{n_y} \otimes \mathbf{I}_{n_x} + \beta_x \mathbf{I}_{n_z} \otimes \mathbf{I}_{n_y} \otimes \mathbf{J}_{n_x}$ , where  $\beta_x, \beta_y$ , and  $\beta_z$  are nonnegative parameters,  $I_k$  is the identity matrix of order  $k$ , and  $J_k$  is the  $k \times k$  tridiagonal matrix with all nonzero off-diagonals as  $-1$ , the first and the last diagonal entries both as  $1$  and the other diagonal entries all as  $2$ . For all practical purpose,  $n = n_x n_y n_z$  is large, and  $\Lambda$  is an enormous but sparse matrix, with each row having at most seven non-zero elements corresponding to the two neighbors in each direction and the voxel itself. The penalty in (4) can be written as the kernel of the (improper) matrix normal density

$$f(\mathbf{W}; \Psi, \beta) = \frac{|\Lambda|_+^{3/2} \exp\left(-\frac{1}{2} \text{Tr} (\Psi^{-1} \mathbf{W}' \Lambda \mathbf{W})\right)}{(2\pi)^{3n/2} |\Psi|^{n/2}}, \quad (5)$$

where  $|\Lambda|_+$  is the product of the positive eigenvalues of  $\Lambda$ . The Kronecker structure in the components of  $\Lambda$  means that  $\Psi$  and  $\beta = (\beta_x, \beta_y, \beta_z)$  need a constraint for identifiability. Though there are many options, we impose the constraint that  $2\beta_x + 2\beta_y + 2\beta_z = 1$ , from the alternative specification of (5) as the (improper) density of a first order intrinsic multi-layer GMRF [44], [47], [48]. If  $\mathbf{W}'_i$  is the  $i$ th row (corresponding to the  $i$ th interior voxel) of  $\mathbf{W}$ , then the conditional distribution of  $\mathbf{W}_i$  given  $\mathbf{W}_{-i}$  (that is, all other rows of  $\mathbf{W}$ ) is trivariate Gaussian with conditional mean and variance

$$\mathbb{E}(\mathbf{W}_i | \mathbf{W}_{-i}) = - \sum_{q \heartsuit i} \Lambda_{iq} \mathbf{W}_q, \quad \text{Var}(\mathbf{W}_i | \mathbf{W}_{-i}) = \Psi, \quad (6)$$

where  $q \heartsuit i$  if and only if voxel  $q$  is a neighbor of voxel  $i$ , and  $\Lambda_{iq}$  is the  $(i, q)$ th element of  $\Lambda$ . Similar expressions exist for boundary voxels. Further,  $\Lambda_{iq} = -\beta_x, -\beta_y$  or  $-\beta_z$  if  $q \heartsuit i$  in the  $x$ -,  $y$ - or the  $z$ -direction, so (6) characterizes  $\mathbb{E}(\mathbf{W}_i | \mathbf{W}_{-i})$  as the weighted average of its neighboring  $\mathbf{W}_q$  values with weights  $\beta_x, \beta_y$  or  $\beta_z$ . The conditional variance is constant.

## B. A matrix-free AECM algorithm for parameter estimation

1) *Background*: Analytical or numerical optimization in (4) is well-nigh impractical because of the intractability introduced by the penalty term. A EM algorithm can conceptually be developed from the generative model of the Rice distribution of the individual  $r_{ij}$ s. Specifically, with  $r_{ij}$  as the observed magnitude, we let  $\theta_{ij}$  be the (missing) direction, then  $(r_{ij} \cos \theta_{ij}, r_{ij} \sin \theta_{ij})$  is bivariate normally distributed with mean  $(\nu_{ij}, 0)$  and variance  $\sigma_j^2 \mathbf{I}$ . Then, ignoring terms not involving  $\nu_{ij}$ , the complete log-likelihood is  $\sum_{i=1}^n \sum_{j=1}^m \sigma_j^{-2} (r_{ij} \nu_{ij} \cos \theta_{ij} - \nu_{ij}^2/2)$ . The algorithm iteratively computes, in the expectation step (E-step), the expectation of the complete loglikelihood given the observations, evaluated at the current parameter values, while the maximization step (M-step) maximizes the result. We now list the two steps.

a) *E-step*:: The E-step requires the conditional expectation of each  $\cos \theta_{ij}$  given  $r_{ij}$  at the current values  $(\mathbf{W}^{(t)}, \Psi^{(t)}, \beta^{(t)})$  of  $(\mathbf{W}, \Psi, \beta)$ . We compute

$$Z_{ij}^{(t)} := \mathbb{E}[\cos \theta_{ij} | r_{ij}; \nu_{ij}^{(t)}] = A_1 \left( \frac{r_{ij} \nu_{ij}^{(t)}}{\sigma_j^2} \right),$$

where  $A_1(x) := \mathbb{I}_1(x)/\mathbb{I}_0(x)$ . Here,  $Z_{ij}^{(t)}$  is free of  $\beta^{(t)}$  or  $\Psi^{(t)}$ , but rather, depends only on  $\nu_{ij}^{(t)}$  which only involves the  $i$ th row of  $\mathbf{W}^{(t)}$ . So  $Z_{ij}^{(t)}$ s can be computed in parallel without any data racing by allocating an instance of  $\sigma_j^2$  to every processor thread.

b) *M-Step*:: At the  $(t+1)$ th iteration, updates  $(\mathbf{W}^{(t+1)}, \Psi^{(t+1)}, \beta^{(t+1)})$  are obtained by maximizing

$$Q^*(\mathbf{W}, \Psi, \beta; \mathbf{W}^{(t)}) = Q(\mathbf{W}; \mathbf{W}^{(t)}) + \log f(\mathbf{W}; \Psi, \Lambda) \quad (7)$$

with respect to  $(\mathbf{W}, \Psi, \beta)$ , with

$$Q(\mathbf{W}; \mathbf{W}^{(t)}) = \sum_{i=1}^n \sum_{j=1}^m \frac{1}{\sigma_j^2} \left( -\frac{\nu_{ij}^2}{2} + r_{ij} \nu_{ij} Z_{ij}^{(t)} \right). \quad (8)$$

In (8),  $\nu_{ij}$  is again a function only of the  $i$ th row of  $\mathbf{W}$ . However, optimization of  $Q^*$  is still challenging so [9] employed an OSL-EM algorithm [38]. Specifically, they solved  $\nabla Q(\mathbf{W} | \mathbf{W}^{(t)}) + \nabla \log f(\mathbf{W}^{(t)}; \Psi, \beta) = 0$  in  $(\mathbf{W}, \Psi, \beta)$ . This equation can be decomposed into those involving only the individual rows of  $\mathbf{W}$ , greatly simplifying computation. (The equations for  $\Psi$  and  $\beta$  are still joint.) However, unlike the EM algorithm, OSL-EM is neither guaranteed to converge, nor increase the penalized log-likelihood monotonically at each iteration (see Figure S1 for an illustration where OSL-EM actually reduces the penalized log-likelihood providing a sub-optimal estimate). So, we describe and implement an AECM algorithm that is guaranteed to converge monotonically to a local maximum.

2) *Development and implementation:* An AECM algorithm [43] partitions the parameter space and splits the maximization step into conditional maximization (CM) steps, one for each element in the above partition, and alternates the E-step with each CM step. In our framework, we exploit the GMRF structure underlying  $\mathbf{W}$  to color the voxels as black or white using a checkerboard pattern [44] so that no two neighboring voxels have the same color. Then our parameter space is partitioned into three sets, with one partition for the  $\mathbf{W}$ s at the black voxels, a second partition for the  $\mathbf{W}$ s at the white voxels and third partition containing  $(\Psi, \beta)$ . Then each partition is updated in its CM-step while keeping the variables in the other partitions fixed at their current values.

Our bifurcation of  $\mathbf{W}$  is driven by the fact that the CM-step for  $\mathbf{W}$  at each black (white) voxel involves fixed values from only the neighboring white (correspondingly black) voxels. So the optimization problems over the black (white) voxels are *embarrassingly* parallel and are efficiently implementable with negligible data race conditions. Our race-negligible parallel optimization is explicitly described by

**Proposition II.1.** *Maximizing  $Q^*(\mathbf{W}, \Psi, \beta; \mathbf{W}^{(t)})$  with respect to  $\mathbf{W}_i$  for fixed  $(\Psi, \beta)$  and other rows of  $\mathbf{W}$  is equivalent to maximizing*

$$Q_i^*(\mathbf{W}_i) = \sum_{j=1}^m \frac{1}{\sigma_j^2} \left( -\nu_{ij}^2/2 + r_{ij}\nu_{ij}Z_{ij}^{(t)} \right) - \sum_{q \heartsuit i} \Lambda_{i,q} \mathbf{W}'_q \Psi^{-1} \mathbf{W}_i - \frac{1}{2} \Lambda_{i,i} \mathbf{W}'_i \Psi^{-1} \mathbf{W}_i \quad (9)$$

with gradient vector with respect to  $\mathbf{W}_i$  given by

$$\nabla Q_i^*(\mathbf{W}_i) = \sum_{j=1}^m \frac{1}{\sigma_j^2} \left( -\nu_{ij} + r_{ij}Z_{ij}^{(t)} \right) \nabla \nu_{i,j} - \sum_{q \heartsuit i} \Lambda_{i,q} \Psi^{-1} \mathbf{W}_q - \Lambda_{i,i} \Psi^{-1} \mathbf{W}_i. \quad (10)$$

Here  $\nabla \nu_{i,j}$  is the gradient vector of  $\nu_{i,j}$  with respect to  $\mathbf{W}_i$ .

*Proof.* See Section S1-A. □

Proposition II.1 yields a small 3D optimization problem that we efficiently solve using the quasi-Newton box-constrained L-BFGS-B algorithm with limited memory calculations for the Hessian matrix [49], [50]. The box constraints are obtained from the ranges of  $(\mathbf{W}_1, \mathbf{W}_2, \mathbf{W}_3)$ . Next, for fixed  $\mathbf{W}$ , we describe how to update the estimates of  $(\Psi, \beta)$ . The following proposition shows that given  $\beta$ ,  $\Psi$  can be analytically profiled out giving a simple objective function only in  $\beta$ .

**Proposition II.2.** *Fix  $\mathbf{W} = \mathbf{W}^{(t+1)}$ . For fixed  $\beta$ , the function  $\Psi \rightarrow Q^*(\mathbf{W}, \Psi, \beta; \mathbf{W})$  is maximized at  $\hat{\Psi} = n^{-1} \mathbf{W}' \Lambda \mathbf{W}$  (note that  $\Lambda \equiv \Lambda(\beta)$ ). The resulting profile function for  $\beta$  is*

$$Q_p^*(\beta) = c + \frac{3}{2} \log |\Lambda|_+ - \frac{n}{2} \log |\mathbf{W}' \Lambda \mathbf{W}| \quad (11)$$

where  $c$  is a constant that depends only on  $n$  but not on  $\beta$ .

*Proof.* See Section S1-B. □

(11) and its derivative require calculation of  $|\Lambda|_+$  and the determinant of a  $3 \times 3$  matrix  $\mathbf{W}' \Lambda \mathbf{W}$ . but these are easily done by noting that the eigenvalues of  $\mathbf{J}_k$  [48] are

$$\lambda_i = 2 \left[ 1 - \cos \left\{ \frac{\pi(i-1)}{k} \right\} \right] \text{ for } i = 1, 2, \dots, k. \quad (12)$$

Let  $\mathbf{D}_k$  be the vector of eigenvalues of  $\mathbf{J}_k$  ( $k = n_x, n_y, n_z$ ). Then  $|\Lambda|_+$  is a product of the elements of the vector  $\beta_x \mathbf{1}_{n_z} \otimes \mathbf{1}_{n_y} \otimes \mathbf{D}_{n_x} + \beta_y \mathbf{1}_{n_z} \otimes \mathbf{D}_{n_y} \otimes \mathbf{1}_{n_x} + \beta_z \mathbf{D}_{n_z} \otimes \mathbf{1}_{n_y} \otimes \mathbf{1}_{n_x}$ . Our matrix-free treatment of  $(\Psi, \beta)$  is a faster, more elegant and easier-implemented contrast to [9] where  $\Psi$  is further parametrized via a Cholesky factorization and updated with  $\beta$  using another L-BFGS-B algorithm.

Like OSL-EM, we initialize the  $\mathbf{W}$  in our AECM algorithm with the LS estimates, and obtain initial values of  $\Psi$  and  $\beta$ , as per Proposition II.2. Our AECM algorithm is guaranteed [43] to converge, as also illustrated in Figure S1.

### C. Generating synthetic images

The estimated  $(\rho, T_1, T_2)$ , obtained from the terminating  $\mathbf{W}$ s, are inserted along with desired design parameter settings into (1) to synthesize spin-echo images. Similar methods can be employed for other MRI pulse sequences.

#### D. Matrix-free computation of SEs of ROIs in synthetic images

An attractive feature of our model-based approach and the use of penalized likelihood estimators is the provision for ready calculation of SEs. Here we provide the theoretical development and fast implementation for calculating SEs of means of regions of interest (ROIs) in synthetic images  $\hat{\nu}$ .

Following [51] or [52], the estimated observed penalized information matrix for  $\mathbf{W}$  is given by  $\hat{\Omega} = \hat{\mathbf{H}} + \hat{\Lambda} \otimes \hat{\Psi}^{-1}$ , where  $\hat{\mathbf{H}}$  is the negative of the Hessian of the observed log-likelihood (3) with respect to  $\mathbf{W}$  evaluated at  $\hat{\mathbf{W}}$  (see Section S1-C),  $\hat{\Lambda}$  is the  $\Lambda$  matrix evaluated at the terminating  $\hat{\beta}$ , and  $\hat{\Psi}$  is also from the terminated AECM algorithm. Thus,  $\hat{\mathbf{H}}$  is a  $3n \times 3n$  block-diagonal matrix (with entries corresponding to the background voxels set to zero). The approximate dispersion matrix of a synthetic image  $\hat{\nu}$  is calculated from  $\hat{\Omega}$  by the multivariate delta method to be  $\mathbf{S} = \nabla \hat{\nu} \hat{\Omega}^{-1} \nabla \hat{\nu}'$  where  $\nabla \hat{\nu}$  is the  $n \times 3n$  Jacobian matrix of  $\nu$  with respect to  $\mathbf{W}$  evaluated at  $\hat{\mathbf{W}}$ . The computation of  $\mathbf{S}$  can be challenging but parallelized. Moreover, in practice, we are mostly interested in calculating means and SEs of ROIs drawn on synthetic images. The SE of a linear combination  $\mathbf{c}'\hat{\nu}$  of the voxel-wise values of a synthetic image is  $\text{SE}(\mathbf{c}'\hat{\nu}) = (\mathbf{c}'\mathbf{S}\mathbf{c})^{1/2} = \{(\mathbf{c}'\nabla \hat{\nu})\hat{\Omega}^{-1}(\nabla \hat{\nu}'\mathbf{c})\}^{1/2}$ .

The computation of  $\text{SE}(\mathbf{c}'\hat{\nu})$  still possesses substantial numerical challenges. In particular, it requires us to solve an equation of the form  $\hat{\Omega}\mathbf{x} = \mathbf{d}$  where  $\mathbf{d} = (\nabla \hat{\nu})'\mathbf{c}$ . Although  $\hat{\Omega}$  is sparse, it is typically so large that standard methods based on sparse matrix factorization (e.g. sparse Cholesky decomposition) run out of memory mainly because they suffer from fill-ins. In our example, even the heuristic methods [53, Ch. 8] for reducing fill-ins failed to provide a factorization in machines with 384GB RAM. So we use the matrix-free Lanczos algorithm [48] to solve the system. Specifically, we initialize as  $\theta_1 = \|\mathbf{d}\|$ ,  $\mathbf{v}_1 = \mathbf{d}/\theta_1$ ,  $\mathbf{w}_1 = \hat{\Omega}\mathbf{v}_1$ ,  $\kappa_1 = \mathbf{v}_1'\mathbf{w}_1$ ,  $\gamma_1 = \sqrt{\kappa_1}$ ,  $\phi_1 = \theta_1/\gamma_1$ ,  $\mathbf{h}_1 = \mathbf{v}_1/\gamma_1$  and set the initial solution:  $\mathbf{x}_1 = \phi_1\mathbf{h}_1$ . Next, for  $i = 2, 3, \dots$ , we

- set  $\theta_i = \|\mathbf{w}_{i-1} - \kappa_{i-1}\mathbf{v}_{i-1}\|$ ,  $\mathbf{v}_i = (\mathbf{w}_{i-1} - \kappa_{i-1}\mathbf{v}_{i-1})/\theta_i$ , and  $\mathbf{w}_i = \hat{\Omega}\mathbf{v}_i - \theta_i\mathbf{v}_{i-1}$ .
- then set  $\kappa_i = \mathbf{v}_i'\mathbf{w}_i$ ,  $\delta_i = \theta_i/\gamma_{i-1}$ ,  $\gamma_i = \sqrt{\kappa_i - \delta_i^2}$ ,  $\phi_i = -\delta_i\phi_{i-1}/\gamma_i$  and  $\mathbf{h}_i = (\mathbf{v}_i - \delta_i\mathbf{h}_{i-1})/\gamma_i$ .
- update the solution:  $\mathbf{x}_i = \mathbf{x}_{i-1} + \phi_i\mathbf{h}_i$ .
- stop if the relative error  $\|\hat{\Omega}\mathbf{x}_i - \mathbf{d}\|/\theta_1$  is smaller than some pre-specified tolerance.

By carefully recycling the memory space for  $\mathbf{v}_i$ s and  $\mathbf{w}_i$ s, the Lanczos algorithm requires only  $O(n)$  memory in addition to the storage for  $\hat{\Omega}$ . Also,  $\hat{\Omega}$  is used only through the matrix-vector product  $\hat{\Omega}\mathbf{v}_i$  which can be computed fast in  $O(n)$  computational complexity. Finally, while we may use an incomplete Cholesky preconditioner to accelerate convergence of the Lanczos iterations [48], our examples showed that a simple diagonal preconditioner achieves the same or better computing speed.

In this section, we have developed a computationally practical AECM algorithm for generating synthetic MR images from as few as three training MR images, and also provided methods for fast estimation of the standard errors of means over ROIs in such images. We now evaluate performance.

### III. PERFORMANCE EVALUATIONS

This section illustrates evaluates performance of our AECM methodology. We first illustrate and evaluate performance on a dataset of images aquired at 12 (TE, TR) settings [9] and then use simulation experiments on a realistic phantom dataset drawn from [54] to assess properties of our estimator in the presence of increasing noise, such as happens with other MR imaging techniques or higher resolution images [55].

#### A. Application to Real Dataset

1) *Experimental framework:* Our AECM methodology was evaluated relative to LS and OSL-EM on 3D magnitude MR images of a normal healthy male volunteer acquired using the spin-echo imaging sequence at 12 (TE,TR) settings [9]. The datasets were acquired on a 1.5T Signa scanner using spin-echo imaging sequence at a resolution of  $1.15\text{mm} \times 1.15\text{mm} \times 7.25\text{mm}$  in a field of view set to be  $294\text{mm} \times 294\text{mm} \times 145\text{mm}$ . For each 3D image volume,  $n_x = n_y = 256$  and  $n_z = 20$ . From the 12 images, we initially chose three images for our training images and used the LS, OSL-EM and AECM algorithms to estimate  $\rho$ ,  $T_1$  and  $T_2$  at each voxel. These estimates were then inserted into (1) along with design parameters corresponding to the remaining nine images. The predicted synthetic images were then compared to the acquired images to evaluate each of the LS, OSL-EM and AECM methods.

For numerical measures, we used the root mean squared prediction error (RMSPE) for the  $j$ th image image volume, given by  $\sqrt{\sum_{i=1}^n (r_{ij} - \hat{\nu}_{ij})^2/n}$ . We also calculated the mean absolute prediction error (MAPE), defined for the  $j$ th image volume as  $\sum_{i=1}^n |r_{ij} - \hat{\nu}_{ij}|/n$ . In order to compare across predicted images obtained at different settings, we scaled the RMSPE by the standard deviation of the foreground voxel values in  $j$ th acquired image. Similarly the MAPE was scaled by the mean absolute deviation from the mean of the foreground voxels of the  $j$ th acquired image. Finally, our evaluations calculated  $\hat{\nu}_{ij}$  from the synthesized  $\nu_{ij}$  in two ways. First, we used  $\hat{\nu}_{ij}$  without accounting for the Rice distribution of the voxel-wise predictions. In the second case, we set  $\hat{\nu}_{ij}^* = \hat{\sigma}_j \sqrt{\pi/2} \mathbb{L}_{1/2}(-\hat{\nu}_{ij}^2/\hat{\sigma}_j^2)$ , or the mean of the Rice distribution with parameters  $\hat{\nu}_{ij}$  and  $\hat{\sigma}_j$ , with  $\mathbb{L}_{1/2}(x) = e^{x/2} [(1-x)\mathbb{I}_0(-x/2) - x\mathbb{I}_1(-x/2)]$  denoting the Laguerre polynomial of order 1/2. Our synthetic images are compared with (observed) images acquired at the design parameter settings, so the use of  $\hat{\nu}^*$ , that accounts for the Ricean noise through the mean, better estimates the forecast error between the observed and the predicted images.



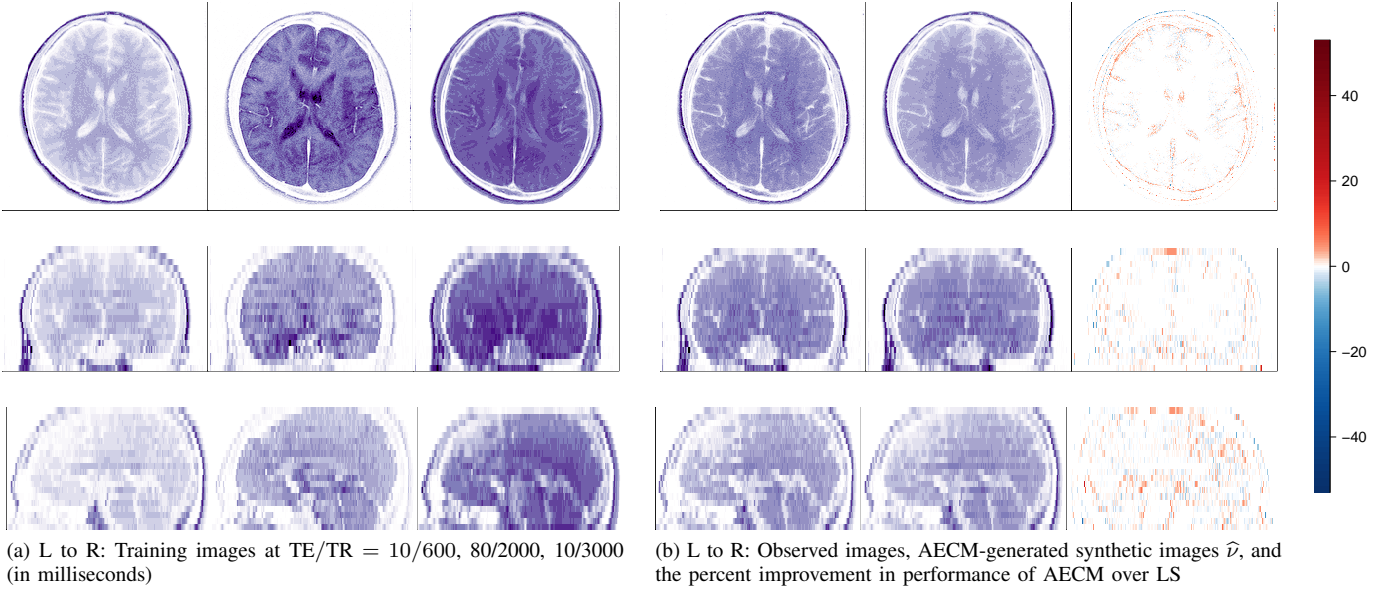


Fig. 1. (a) Mid-axial (top), mid-coronal (middle), and mid-sagittal (bottom) views for the training images and (b) observed and AECM-synthesized image at the median-performing (out of nine, in terms of RMSPE) design parameter setting.

2) *Results:* We now discuss results of our experiments done as per Section III-A1. Computations were done in parallel on a 2.3GHz Intel(R) Xeon(R) Gold 6140 processor, capable of handling up to 36 threads.

a) *Illustration of AECM methodology for synthetic MRI:* We first illustrate performance of our AECM on the three training images of Fig. 1 that were acquired at  $(TE, TR) \in \{(10, 600), (80, 2000), (10, 3000)\}$  (all times are in milliseconds). Fig. S1 shows the objective function in (4) as the OSL-EM and AECM algorithms proceed from LS initialization. In this example, OSL-EM is seen to have an uncertain trajectory, and on the whole, goes down after the first iteration. On the other hand, AECM correctly increases and terminates in a few iterations. Our implementation of AECM ensures that this accuracy does not come at a price, with estimation and synthetic image generation typically done in seconds. We now discuss performance.

Fig. 1b displays performance of AECM in synthesizing MR images at the median (in terms of the median RMPSE) of the nine design parameter settings. The figures indicate fairly accurate reproduction by the AECM-estimated synthetic images. This finding is further vindicated by Table I which displays accuract of prediction at all settings. Also, Fig. 1b displays the

TABLE I  
THE 12 (TE, TR) (IN MILLISECONDS AND SECONDS RESPECTIVELY) SETTINGS ALONG WITH THE SCALED RMSPE AND MAPE FOR THE BEST TRAINING SET (SCALE:  $\times 0.01$ ).

Settings	j	1	2	3	4	5	6	7	8	9	10	11	12
TE	10	15	20	10	30	40	10	40	80	10	60	100	
TR	0.6	0.6	0.6	1.0	1.0	1.0	2.0	2.0	2.0	3.0	3.0	3.0	
RMSPE	$\hat{v}$	3.23	13.65	15.94	16.90	19.22	21.20	33.65	18.78	1.14	1.74	20.73	28.29
	$\hat{v}^*$	3.22	13.66	15.97	16.89	19.24	21.22	33.62	18.78	1.15	1.75	20.72	28.21
MAPE	$\hat{v}$	6.94	15.71	18.12	21.02	22.28	24.04	43.85	21.55	4.94	3.52	24.14	33.32
	$\hat{v}^*$	6.96	15.72	18.15	21.01	22.30	24.06	43.81	21.56	4.94	3.55	24.13	33.26

voxel-wise difference in the absolute deviation of the AECM predictions from the test images, and the LS predictions from the test images, and shows overall improvement. (The overall numerical improvement of AECM over LS in this example is quantified a little later in Table II.)

b) *Choice of Optimal Training Set:* Following [9], we also investigate all possible (TE, TR) settings to see if some choice can provide better synthetic images. There are  ${}^{12}C_3 = 220$  possible sets of three training images, but some of them are not distinct and are discarded, leaving behind 212 sets. For each set of three training images, we obtained LS, OSL-EM and AECM-estimated parameters and then obtained synthetic images for the nine (TE, TR)-values outside the considered training set.

Table II displays numerical performance of the AECM-estimated synthetic images for the top 10 combinations (ordered according to the increasing scaled RMSPE), and shows the per cent improvement of AECM and OSL-EM over LS for each of the measures. We see around 5% improvement of AECM over LS. Once again, OSL-EM is unpredictable in its improvement over LS, often doing worse.

TABLE II

THE TEN BEST TRAINING SETS, THEIR PERFORMANCE MEASURES FOR THE LS ESTIMATES, AND THEIR AVERAGE PERFORMANCE MEASURES RELATIVE TO THE LS ESTIMATES ( $\times 0.01$ ). IN THE TABLE, OSL AND AE DENOTE OSL-EM AND AECM-ESTIMATED PREDICTIONS.

Training	LS performance measure				RMSPE				MAPE			
	RMSPE		MAPE		$\hat{d}$		$\hat{d}^*$		$\hat{d}$		$\hat{d}^*$	
	$\hat{d}$	$\hat{d}^*$	$\hat{d}$	$\hat{d}^*$	OSL	AE	OSL	AE	OSL	AE	OSL	AE
Images												
1, 9, 10	20.93	20.92	24.89	24.89	-0.44	1.10	-0.34	1.98	-0.26	1.28	0.01	1.20
2, 9, 10	21.11	21.10	25.08	25.07	-0.64	1.28	-0.50	2.41	-0.47	1.49	-0.09	1.44
2, 10, 12	21.60	21.60	25.71	25.70	-1.19	0.95	-1.54	1.76	-1.21	1.00	-0.80	0.95
2, 7, 9	21.38	21.35	25.34	25.32	0.68	3.42	1.53	6.55	1.23	3.51	1.32	3.44
1, 10, 12	21.64	21.64	25.77	25.77	-0.90	1.12	-1.26	1.92	-1.09	1.15	-0.81	1.03
1, 7, 9	21.54	21.54	25.54	25.54	0.14	2.97	0.77	5.78	0.65	2.96	0.87	2.94
1, 8, 9	21.54	21.53	24.97	24.96	0.19	3.82	0.85	7.36	-0.12	3.46	0.10	3.41
1, 10, 11	21.86	21.83	25.83	25.81	0.02	1.05	0.57	2.01	0.15	1.08	0.36	1.05
2, 10, 11	21.91	21.89	25.89	25.86	-0.21	1.27	0.26	2.44	-0.13	1.43	0.19	1.40
2, 8, 9	21.60	21.59	25.05	25.04	-0.00	3.24	0.59	6.35	-0.38	3.03	-0.09	3.02

TABLE III

THE PERFORMANCE MEASURES (AVERAGE RMSPE AND MAPE, IN %) OF THE BEST TRAINING SAMPLES FOR DIFFERENT TRAINING SET SIZES FOR THE REAL DATASET.

m	3	4	5	6	7	8	9	10	11
RMSPE	20.93	19.56	17.28	16.30	14.94	14.43	13.83	13.29	13.07
MAPE	24.89	22.60	19.93	18.74	17.24	16.76	16.01	15.46	15.14

c) *Consistency of Predictions*:: A desirable feature of any estimation or prediction method is statistical consistency, or improvement in performance as more information (training image set) becomes available. Therefore, we considered and evaluated performance of the AECM method in generating synthetic images as the number of images in the training set increased over  $m \in \{3, 4, 5, \dots, 11\}$ . For each  $m$ , we evaluated predictive performance with a training set of images of all possible training image set combinations of size  $m$  and compared them with the remaining images in the test sample. Table III shows the RMSPE and MAPE values for the best set for each  $m$ , and shows prediction consistency of our synthetic MRI approach.

3) *Estimating SEs of ROI means*: Our final set of evaluations is on estimating SEs of ROI means in synthetic images obtained using the training set in Fig. 1. We considered three ROIs consisting of Cerebro-Spinal Fluid (CSF), Gray Matter (GM) and White Matter (WM). Table IV provides the ROI means of the synthetically generated variances. The machinery of Section II-D was used to estimate SEs of the ROI means and compared with computationally expensive bootstrap estimates. (For details, see Section S2-B, which also shows insignificant differences between our estimates and the bootstrap-estimated SEs.)

TABLE IV

ESTIMATED CSF, GM AND WM ROI MEANS IN SYNTHETIC IMAGES AND THEIR SEs:  $\hat{\sigma}_s$ S CALCULATED USING THE FORMULA IN SECTION II-D, AND  $\hat{\sigma}_b$ S ESTIMATED USING PARAMETRIC BOOTSTRAP. THE SCALE FOR THE SEs IS  $\times 10^{-3}$ .

Image	CSF			GM			WM		
	Mean	$\hat{\sigma}_s$	$\hat{\sigma}_b$	Mean	$\hat{\sigma}_s$	$\hat{\sigma}_b$	Mean	$\hat{\sigma}_s$	$\hat{\sigma}_b$
2	36.7	3.73	4.45	73.1	3.31	3.71	123.4	7.53	6.93
3	33.8	3.95	4.15	67.9	3.05	3.41	111.4	7.07	6.61
4	57.7	5.11	5.62	112.7	4.09	4.62	167.1	7.73	7.38
5	42.0	4.13	4.35	84.0	2.99	3.28	110.5	6.22	6.07
6	36.3	3.85	4.07	72.8	2.74	2.95	90.0	6.44	6.52
7	88.4	5.55	5.70	164.0	3.96	4.23	191.4	9.86	9.52
8	55.9	4.44	4.51	106.4	2.79	2.77	102.7	7.21	7.24
11	52.6	5.42	5.41	93.4	3.59	3.73	69.8	7.44	7.80
12	33.3	5.13	4.69	54.5	3.39	3.49	31.1	5.74	6.18

## B. Simulation Experiments

Our next set of experiments is on estimation and prediction accuracy relative to noise. Because there is no way to acquire true  $\rho$ ,  $T_1$  and  $T_2$  images from real data, estimation accuracy can only be evaluated by means of simulation experiments. At the same time, it is not feasible to obtain several real datasets using higher resolutions or MRI pulse sequences that have lower signal-to-noise ratios (SNR) [55] than the spin-echo technique, so we also use simulation to get a sense of prediction performance in such settings.

Our ground truth for  $\rho$ ,  $T_1$  and  $T_2$  images were obtained from the Brainweb interface of [54] that allows for the simulation of realistic images at different TE and TR settings, different slice thicknesses, noise levels or intensity non-uniformity levels.

We obtained “noiseless” images using a simulated spin-echo sequence at six different (TE, TR) settings: (30, 3000), (80, 3000), (10,35), (10, 3000), (10, 600), (80, 2000) and then inverted them using LS to get the ground truth for  $\rho$ ,  $T_1$  and  $T_2$  images. Mid-axial, coronal, and sagittal views of these ground truths are in the first columns of Figs. 2a, b and c. We inserted these  $\rho$ ,  $T_1$  and  $T_2$  images into (1) at the three training image (TE, TR) settings of Table I to get the noiseless signal at that setting that was corrupted with Ricean noise (2) for a given  $\sigma$  that was chosen according to the desired average SNR. The average SNR was calculated by averaging the voxelwise SNRs over the foreground voxels. Given the true signal  $\nu_{ij}$  at the  $i$ th voxel and  $j$ th design parameter setting as in (1), the variance  $\varsigma_{ij}^2$  at that voxel is  $\varsigma_{ij}^2 = 2\sigma^2 + \nu_{ij}^2 - \pi\sigma^2\mathbb{L}_{1/2}^2(-\nu_{ij}^2/2\sigma^2)/2$ , following properties of the Rice distribution (2). The SNR at the  $i$ th voxel for the image with  $j$ th design parameter setting (TE $_j$ , TR $_j$ ) is then  $\nu_{ij}/\varsigma_{ij}$ .

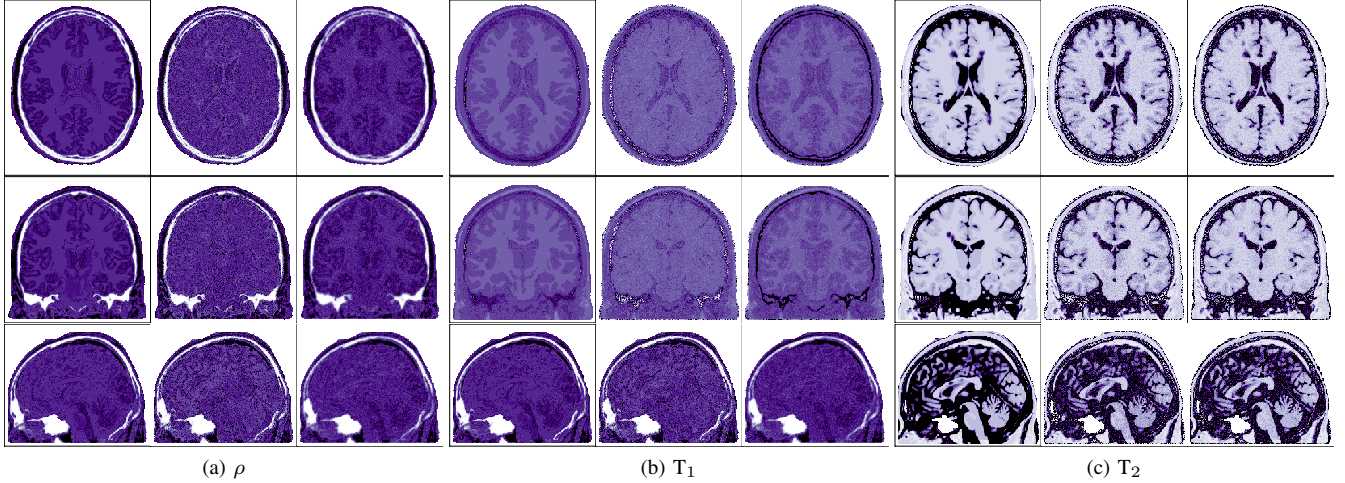


Fig. 2. Mid-axial (top), mid-coronal (middle), and mid-sagittal (bottom) views of  $\rho$ ,  $T_1$  and  $T_2$  for the Brainweb-based simulation with average SNR of 8.25. In each view, the first column corresponds to the ground truth physical quantity while the next two columns correspond to its LS and AECM estimates.

Our three simulated training images in Fig. 2 had average SNRs of 66.45, 73.76, 100.07, corresponding to  $\sigma = 1.99, 1.56, 2.72$ . These three images were then used to obtain LS and AECM estimates of  $\rho, T_1, T_2$ , as shown in Fig. 2. We see that the AECM estimates recover the ground truths quite accurately and better on the whole than LS which cannot always estimate the detailed spatial structure. We also obtained numerical performance measures through the root mean squared error (RMSE) of the estimates. Table Va provides the RMSEs of the LS and AECM estimates with differing average SNR. We used  $W$  in these calculations since our estimation was done in that space. As in Fig. 2, Table Va demonstrates improved estimation accuracy with AECM over LS estimation. It shows that the penalized method always provides better estimates of  $W_1$  and  $W_2$ . Although, LS appears to provide better estimates of  $W_3$  than at unrealistically high SNR settings, the difference in the errors is only marginal. This is also reflected by the uniformly better prediction accuracy of the penalized method, as described below. Also, estimation error decreases faster with increasing SNR under AECM than LS (Fig. S2).

TABLE V  
(A) ESTIMATION AND (B) PREDICTION ERROR AND CONSISTENCY OF LS AND AECM METHODS IN THE SIMULATION EXPERIMENTS.

Avg.	$W_1$		$W_2(\times 0.1)$		$W_3(\times 10^{-3})$		RMSPE		MAPE	
	LS	AECM	LS	AECM	LS	AECM	LS	AECM	LS	AECM
80.09	26.24	6.45	1.11	0.79	1.32	1.42	0.045	0.017	0.066	0.020
16.18	34.83	24.26	1.45	1.14	1.86	1.86	0.101	0.082	0.121	0.099
8.25	49.82	38.47	1.72	1.47	2.17	2.19	0.179	0.157	0.213	0.190
4.37	74.57	50.19	2.13	1.88	2.61	2.45	0.337	0.280	0.400	0.337
2.34	119.95	93.22	2.75	2.48	3.63	2.74	0.767	0.544	0.912	0.646
2.06	138.90	121.57	3.01	2.52	4.06	2.82	1.134	0.672	1.329	0.793
1.98	151.30	136.98	3.23	2.84	4.39	2.70	1.515	0.804	1.716	0.939

(a) Estimation error of  $W_1, W_2, W_3$

(b) Prediction error of synthetic images

Since the main objective of synthetic MRI is the synthesizing of images at unobserved design parameter settings, we also compared the predicted synthetic images at the nine additional (unshaded) (TE, TR) values in Table I. Table Vb reports the average (over the nine design parameter settings) RMSPE and MAPE of the predicted synthetic MRIs vis-a-vis those obtained by inserting the ground truth in (1). We see that the AECM provides better prediction accuracy than LS at a given setting, providing confidence in the use of our technique in low-SNR situations such as images obtained at higher resolutions or with



other MRI pulse sequences than the spin-echo technique. Additionally, Table Vb also shows prediction error decreases faster with increasing SNR under AECM than LS (Fig. S3).

Our performance evaluations indicate that our AECM approach can improve synthetic MRI. Unlike machine learning approaches, our model-based approach can be applied to situations that are specific to individual patients and scanners and can be used to synthesize images at any design parameters.

#### IV. DISCUSSION

We have provided a computationally practical but theoretically sound implementation of model-based synthetic MR imaging that can enable its use patient-specific settings. Our approach penalizes the Rice-distribution based loglikelihood through a transformed GMRF [9] with parameters estimated via a matrix-free AECM scheme, that unlike OSL-EM, is guaranteed to solve (4) locally. Experimental evaluations show it to have better overall performance over LS-based synthetic MR methods at minor additional cost. An added benefit of our model-based approach is the ready availability of SE estimates, for which we also provide practical matrix-free computations. Our experiments show that our estimates are nonsignificantly distinct from those obtained using bootstrap procedures.

There are some issues that could benefit from further attention. For instance, transformations beyond the ones used in transforming  $(\rho, T_1, T_2)$  to  $(W_1, W_2, W_3)$  could be investigated. Also of interest may be the choice of penalty functions that go beyond stationary GMRFs. The use of practical Bayesian methodology incorporating ingredients of our matrix-free approach may also be worth exploring.

#### SOFTWARE

Software in the form of a C++ library and package with R and Matlab interfaces, together with a sample input data set and complete documentation is available at <https://github.com/StatPal/symr>.

#### REFERENCES

- [1] L. M. Katims, "Nuclear magnetic resonance imaging: methods and current status," *Medical Instrum.*, vol. 16, no. 4, pp. 213–6, 1982.
- [2] P. Mansfield and P. G. Morris, *NMR Imaging in Biomedicine*. New York: Academic Press, 1982.
- [3] W. S. Hinshaw and A. H. Lent, "An introduction to NMR imaging: From the bloch equation to the imaging equation," *Proceedings of the IEEE*, vol. 71, no. 3, pp. 338–350, 1983.
- [4] S. C. L. Deoni, T. M. Peters, and B. K. Rutt, "High-resolution  $T_1$  and  $T_2$  mapping of the brain in a clinically acceptable time with DESPOT1 and DESPOT2," *Magnetic Resonance in Medicine*, vol. 53, pp. 237–241, 2005.
- [5] J. B. M. Warntjes, O. D. Leinhard, J. West, and P. Lundberg, "Rapid Magnetic Resonance quantification on the brain: Optimization for clinical usage," *Magnetic Resonance in Medicine*, vol. 60, pp. 320–329, 2008.
- [6] V. Kuperman, *Magnetic Resonance Imaging: Physical Principles and Applications*, 1st ed. San Diego, California: Academic Press, 2000.
- [7] M. A. Bernstein, K. F. King, and X. J. Zhou, Eds., *Handbook of MRI Pulse Sequences*. Burlington: Academic Press, 2004.
- [8] R. W. Brown, Y.-C. N. Cheng, E. M. Haacke, M. R. Thompson, and R. Venkatesan, Eds., *Magnetic Resonance Imaging: Physical Principles and Sequences*, 2nd ed. Hoboken, New Jersey: John Wiley & Sons, Ltd, 2014.
- [9] R. Maitra and J. J. Riddles, "Synthetic magnetic resonance imaging revisited," *IEEE Transactions on Medical Imaging*, vol. 29, no. 3, pp. 895–902, march 2010.
- [10] R. M. Henkelman, "Measurement of signal intensities in the presence of noise in mr images," *Medical Physics*, vol. 12, no. 2, pp. 232–233, 1985.
- [11] J. Sijbers, "Signal and noise estimation from magnetic resonance images," Ph.D. dissertation, University of Antwerp, 1998.
- [12] J. Sijbers, A. J. den Dekker, J. Van Audekerke, M. Verhoye, and D. Van Dyck, "Estimation of the noise in magnitude MR images," *Magnetic Resonance Imaging*, vol. 16, no. 1, pp. 87–90, 1998.
- [13] S. O. Rice, "Mathematical analysis of random noise," *Bell System Techn. J.*, vol. 23, pp. 282–332, 1944.
- [14] —, "Mathematical analysis of random noise," *Bell System Techn. J.*, vol. 24, pp. 46–156, 1945.
- [15] Yue Wang and Tianhu Lei, "Statistical analysis of MR imaging and its applications in image modeling," in *Proceedings of 1st International Conference on Image Processing*, vol. 1, 1994, pp. 866–870.
- [16] R. Maitra and D. Faden, "Noise estimation in magnitude MR datasets," *IEEE Transactions on Medical Imaging*, vol. 28, no. 10, pp. 1615–1622, 2009.
- [17] R. Maitra, "On the expectation-maximization algorithm for Rice-Rayleigh mixtures with application to estimating the noise parameter in magnitude MR datasets," *Sankhyā: The Indian Journal of Statistics, Series B*, vol. 75, no. 2, p. 293–318, 2013.
- [18] E. L. Hahn, "Spin echoes," *Physical review*, vol. 80, no. 4, p. 580, 1950.
- [19] J. Hennig, A. Nauerth, and H. Friedburg, "RARE imaging – a fast imaging method for clinical MR," *Magnetic Resonance in Medicine*, vol. 3, no. 6, pp. 823–33, 1986.
- [20] H. B. W. Larsson, J. Frederiksen, J. Petersen, A. Nordenbo, I. Zeeberg, O. Henriksen, and J. Olesen, "Assessment of demyelination, edema, and gliosis by *in vivo* determination of  $T_1$  and  $T_2$  in the brain of patients with acute attack of multiple sclerosis," *Magnetic Resonance in Medicine*, vol. 11, no. 3, pp. 337–348, 1989.
- [21] P. Williamson, D. Pelz, H. Merskey, S. Morrison, S. Karlik, D. Drost, T. Carr, and P. Conlon, "Frontal, temporal, and striatal proton relaxation times in schizophrenic patients and normal comparison subjects," *Am J Psychiatry*, vol. 149, no. 4, pp. 549–551, 1992.
- [22] A. Pitkänen, M. Laakso, R. Kälviäinen, K. Partanen, P. Vainio, M. Lehtovirta, P. Riekkinen, and H. Soininen, "Severity of hippocampal atrophy correlates with the prolongation of MRI  $T_2$  relaxation time in temporal lobe epilepsy but not in alzheimer's disease," *Neurology*, vol. 46, no. 6, pp. 1724–1730, 1996.
- [23] J. Vymazal, A. Righini, R. A. Brooks, M. Canesi, C. Mariani, M. Leonardi, and G. Pezzoli, "T1 and T2 in the brain of healthy subjects, patients with parkinson disease, and patients with multiple system atrophy: relation to iron content," *Radiology*, vol. 211, no. 2, pp. 489–495, 1999.
- [24] G. Bartzokis, D. Sultzer, J. Cummings, L. E. Holt, V. W. Hance, D B ad Henderson, and J. Mintz, "*In vivo* evaluation of brain iron in alzheimer disease using magnetic resonance imaging," *Archives of General Psychiatry*, vol. 57, no. 1, pp. 47–53, 2000.
- [25] S. D. Friedman, D. W. Shaw, A. A. Artru, T. L. Richards, J. Gardner, G. Dawson, S. Posse, and S. R. Dager, "Regional brain chemical alterations in young children with autism spectrum disorder," *Neurology*, vol. 60, pp. 100–107, 2003.
- [26] S. Bobman, S. Riederer, J. Lee, S. Suddarth, H. Wang, and J. MacFall, "Synthesized MR images: Comparison with acquired images," *Radiology*, vol. 155, pp. 731–8, 1985.

- [27] S. Bobman, S. Riederer, J. Lee, T. Tasciyan, F. Farzaneh, and H. Wang, "Pulse sequence extrapolation with acquired images," *Radiology*, vol. 159, pp. 253–8, 1986.
- [28] D. A. Feinberg, C. M. Mills, J. P. Posin, D. A. Ortendahl, N. M. Hylton, L. E. Crooks, J. C. Watts, L. Kaufman, M. Arakawa, J. C. Hoenninger, and M. Brantz-Zawadzki, "Multiple spin-echo Magnetic Resonance Imaging," *Radiology*, vol. 155, pp. 437–42, 1985.
- [29] D. A. Ortendahl, Hylton, L. Kaufman, J. C. Watts, L. E. Crooks, and D. D. Stark, "Analytical tools for Magnetic Resonance Imaging," *Radiology*, vol. 153, no. 2, pp. 479–488, 1984.
- [30] F. G. Gonçalves, S. D. Serai, and G. Zuccoli, "Synthetic brain MRI: review of current concepts and future directions," *Topics in Magnetic Resonance Imaging*, vol. 27, no. 6, pp. 387–393, 2018.
- [31] A. M. Betts, J. L. Leach, B. V. Jones, B. Zhang, and S. Serai, "Brain imaging with synthetic mr in children: clinical quality assessment," *Neuroradiology*, vol. 58, no. 10, pp. 1017–1026, 2016.
- [32] A. McAllister, J. Leach, H. West, B. Jones, B. Zhang, and S. Serai, "Quantitative synthetic MRI in children: normative intracranial tissue segmentation values during development," *American Journal of Neuroradiology*, vol. 38, no. 12, pp. 2364–2372, 2017.
- [33] C. Andica, A. Hagiwara, M. Hori, K. Kamagata, S. Koshino, T. Maekawa, M. Suzuki, H. Fujiwara, M. Ikeno, T. Shimizu *et al.*, "Review of synthetic MRI in pediatric brains: Basic principle of mr quantification, its features, clinical applications, and limitations," *Journal of Neuroradiology*, vol. 46, no. 4, pp. 268–275, 2019.
- [34] A. Hagiwara, M. Hori, K. Yokoyama, M. Takemura, C. Andica, T. Tabata, K. Kamagata, M. Suzuki, K. Kumamaru, M. Nakazawa *et al.*, "Synthetic MRI in the detection of multiple sclerosis plaques," *American Journal of Neuroradiology*, vol. 38, no. 2, pp. 257–263, 2017.
- [35] I. K. Glad and G. Sebastiani, "A Bayesian approach to synthetic Magnetic Resonance Imaging," *Biometrika*, vol. 82, no. 2, pp. 237–250, June 1995.
- [36] R. Maitra and J. E. Besag, "Bayesian reconstruction in synthetic Magnetic Resonance Imaging," in *Bayesian Inference in Inverse Problems*, ser. Proceedings of the Society of Photo-Optical Instrumentation Engineers (SPIE) Meetings, A. Mohammad-Djafari, Ed., vol. 3459, 1998, pp. 39–47.
- [37] S. Geman and D. E. McClure, "Bayesian image analysis: Application to single photon emission computed tomography," *Proc. Stat. Comp. Sec., Am. Stat. Assoc.*, pp. 12–18, 1985.
- [38] P. J. Green, "On the use of the EM algorithm for penalized likelihood estimation," *Journal of the Royal Statistical Society, Series B (Methodological)*, vol. 52, pp. 443–452, 1990.
- [39] A. Hagiwara, Y. Otsuka, M. Hori, Y. Tachibana, K. Yokoyama, S. Fujita, C. Andica, K. Kamagata, R. Irie, S. Koshino *et al.*, "Improving the quality of synthetic flair images with deep learning using a conditional generative adversarial network for pixel-by-pixel image translation," *American Journal of Neuroradiology*, vol. 40, no. 2, pp. 224–230, 2019.
- [40] M. Mirza and S. Osindero, "Conditional generative adversarial nets," *arXiv preprint arXiv:1411.1784*, 2014.
- [41] A. Hagiwara, M. Warntjes, M. Hori, C. Andica, M. Nakazawa, K. K. Kumamaru, O. Abe, and S. Aoki, "Symri of the brain: rapid quantification of relaxation rates and proton density, with synthetic MRI, automatic brain segmentation, and myelin measurement," *Investigative radiology*, vol. 52, no. 10, p. 647, 2017.
- [42] S. U. Dar, M. Yurt, L. Karacan, A. Erdem, E. Erdem, and T. Çukur, "Image synthesis in multi-contrast MRI with conditional generative adversarial networks," *IEEE Transactions on Medical Imaging*, vol. 38, no. 10, pp. 2375–2388, 2019.
- [43] X.-L. Meng and D. Van Dyk, "The EM algorithm—an old folk-song sung to a fast new tune," *Journal of the Royal Statistical Society: Series B (Statistical Methodology)*, vol. 59, no. 3, pp. 511–567, 1997.
- [44] J. Besag, "Spatial interaction and the statistical analysis of lattice systems," *Journal of the Royal Statistical Society: Series B (Methodological)*, vol. 36, no. 2, pp. 192–225, 1974.
- [45] J. Besag, P. Green, D. Higdon, and K. Mengersen, "Bayesian computation and stochastic systems," *Statistical Science*, vol. 10, no. 1, pp. 3–41, 1995.
- [46] R Core Team, *R: A Language and Environment for Statistical Computing*, R Foundation for Statistical Computing, Vienna, Austria, 2020. [Online]. Available: <https://www.R-project.org/>
- [47] J. Besag and C. Kooperberg, "On conditional and intrinsic autoregressions," *Biometrika*, vol. 82, no. 4, pp. 733–746, 1995.
- [48] S. Dutta and D. Mondal, "An h-likelihood method for spatial mixed linear models based on intrinsic auto-regressions," *Journal of the Royal Statistical Society: Series B (Statistical Methodology)*, vol. 77, pp. 699–726, 2015.
- [49] R. H. Byrd, P. Lu, and J. Nocedal, "A limited memory algorithm for bound constrained optimization," *SIAM Journal in Scientific and Statistical Computing*, vol. 16, no. 5, pp. 1190–1208, 1995.
- [50] C. Zhu, R. H. Byrd, P. Lu, and J. Nocedal, "Algorithm 778: L-BFGS-B: Fortran subroutines for large-scale bound-constrained optimization," *ACM Transactions on Mathematical Software*, vol. 23, no. 4, pp. 550–560, 1997.
- [51] M. R. Segal, P. Bacchetti, and N. P. Jewell, "Variances for maximum penalized likelihood estimates obtained via the EM algorithm," *Journal of the Royal Statistical Society: Series B (Methodological)*, vol. 56, no. 2, pp. 345–352, 1994.
- [52] W. Lee and Y. Pawitan, "Direct calculation of the variance of maximum penalized likelihood estimates via EM algorithm," *The American Statistician*, vol. 68, no. 2, pp. 93–97, 2014.
- [53] T. A. Davis, *Direct methods for sparse linear systems*. SIAM, 2006.
- [54] C. Cocosco, V. Kollokian, R. Kwan, and A. Evans, "Brainweb: Online interface to a 3d MRI simulated brain database," *NeuroImage*, vol. 5, no. 4, May 1997.
- [55] N. A. Lazar, *The Statistical Analysis of Functional MRI Data*. Springer, 2008.
- [56] K. V. Mardia, J. T. Kent, and J. M. Bibby, *Multivariate Analysis*. Academic Press Inc., 1979.

SUPPLEMENTARY MATERIALS  
S1. SUPPLEMENT TO SECTION II

A. Proof of Proposition II.1

Only the kernel of  $f(\mathbf{W}; \Psi, \Lambda)$  in (5) involves  $\mathbf{W}$  so we have, but for a constant free of  $\mathbf{W}$ ,

$$\log f(\mathbf{W}; \Psi, \Lambda) = -\frac{1}{2} \text{Tr} (\Psi^{-1} \mathbf{W}' \Lambda \mathbf{W}) = -\frac{1}{2} \text{Tr} (\Lambda (\mathbf{W} \Psi^{-1} \mathbf{W}')) = -\frac{1}{2} \sum_p \sum_q \Lambda_{p,q} \cdot \mathbf{W}_q \Psi^{-1} \mathbf{W}'_p. \quad (\text{S1})$$

The portion of (S1) that involves the  $i$ th voxel, and hence  $\mathbf{W}_i$ , is

$$\log f(\mathbf{W}; \Psi, \Lambda) = c - \left( \sum_{q \neq i} \Lambda_{i,q} \mathbf{W}_q \right) \Psi^{-1} \mathbf{W}'_i - \frac{1}{2} \Lambda_{i,i} \mathbf{W}'_i \Psi^{-1} \mathbf{W}_i \quad (\text{S2})$$

which gives us equation (9), with  $c$  a constant not depending on  $\mathbf{W}_i$ . However,  $\Lambda \neq \mathbf{0}$  only if  $q \heartsuit i$ . Applying the chain rule for derivatives, we get the first partial derivative, w.r.t.  $W_{ik}$ , of the  $Q(\mathbf{W}; \mathbf{W}^{(t)})$  of (8) as

$$\frac{\partial Q}{\partial W_{ik}} = \sum_{j=1}^m \sigma_j^{-2} \left( -\nu_{ij} + r_{ij} Z_{ij}^{(t)} \right) \frac{\partial \nu_{ij}}{\partial W_{ik}}, \quad (\text{S3})$$

for which, we need the derivatives of (1). For the transformed variable  $\mathbf{W}$ , the Bloch equation is

$$\nu_{ij} = W_{i1} \left\{ 1 - W_{i2}^{\text{TR}_j} \right\} W_{i3}^{\text{TE}_j} \quad (\text{S4})$$

which yields the derivatives:

$$\frac{\partial \nu_{ij}}{\partial W_{ik}} = \begin{cases} W_{i3}^{\text{TE}_j} \left\{ 1 - W_{i2}^{\text{TR}_j} \right\}, & k=1 \\ -W_{i1} \text{TR}_j W_{i3}^{\text{TE}_j} W_{i2}^{\text{TR}_j-1}, & k=2 \\ W_{i1} \text{TE}_j W_{i3}^{\text{TE}_j-1} \left\{ 1 - W_{i2}^{\text{TR}_j} \right\}, & k=3 \end{cases}$$

and the second derivatives:

$$\frac{\partial^2 \nu_{ij}}{\partial W_{ik} \partial W_{ik'}} = \begin{cases} 0, & k=1, k'=1 \\ -\text{TR}_j W_{i3}^{\text{TE}_j} W_{i2}^{\text{TR}_j-1}, & k=1, k'=2 \\ \text{TE}_j W_{i3}^{\text{TE}_j-1} (1 - W_{i2}^{\text{TR}_j}), & k=1, k'=3 \\ -W_{i1} \text{TR}_j (\text{TR}_j - 1) W_{i3}^{\text{TE}_j} W_{i2}^{\text{TR}_j-2}, & k=2, k'=2 \\ -W_{i1} \text{TR}_j \text{TE}_j W_{i3}^{\text{TE}_j-1} W_{i2}^{\text{TR}_j-1}, & k=2, k'=3 \\ W_{i1} \text{TE}_j (\text{TE}_j - 1) W_{i3}^{\text{TE}_j-2} (1 - W_{i2}^{\text{TR}_j}), & k=3, k'=3. \end{cases}$$

From the above, we get (10) from (S3) and (S2). □

*Remarks:*

- 1) The first line of (S2) inside the parenthesis is needed to only be computed once per iteration per voxel using a sparse iterator and the second line can be computed many times inside the L-BFGS-B algorithm as the algorithm explores the space.
- 2) To have more stable ratios of Bessel functions in the expression for  $Z_{ij}^{(t)}$ , we have used exponentially tilted Bessel functions, and resorted to a Taylor series expansion as the argument tends to  $\infty$ .

B. Proof of Proposition II.2

From (5), we have

$$\log f(\mathbf{W}; \Psi, \beta) = -\frac{1}{2} \text{Tr} (\Psi^{-1} \mathbf{W}' \Lambda \mathbf{W}) + \frac{3}{2} \log |\Lambda|^* - \frac{3n}{2} \log(2\pi) - \frac{n}{2} \log |\Psi| = -\frac{1}{2} \text{Tr} (\Psi^{-1} \Xi) - \frac{n}{2} \log |\Psi| + K, \quad (\text{S5})$$

where  $\Xi = (\mathbf{W}' \Lambda \mathbf{W})$  and  $K$  depends only on  $\beta$  and  $n$ .

The optimization of S5 w.r.t.  $\Psi$  is similar to the problem for finding the maximum likelihood estimator for the variance-covariance matrix in multivariate normal samples as in [56, Theorem 4.2.1]. In our case, the first two terms contain the arithmetic (AM) and the geometric means (GM) of eigenvalues of  $n^{-1} \Psi^{-1} \Xi$ . The AM-GM inequality shows that this expression is maximized at  $\Psi = \Xi/n = (\mathbf{W}' \Lambda \mathbf{W})/n$ . Incorporating this estimated value yields the profile likelihood

$$Q_p^*(\beta) = -\frac{1}{2} \text{Tr} (n \mathbf{I}_3) + \frac{3}{2} \log |\Lambda|^* - \frac{3n}{2} \log(2\pi) - \frac{n}{2} \log \left| \frac{1}{n} \Xi \right| = c + \frac{3}{2} \log |\Lambda|^* - \frac{n}{2} \log |\mathbf{W}' \Lambda \mathbf{W}| \quad (\text{S6})$$

where  $c$  is a constant that involves  $n$ . □

### C. Information Matrix

The observed information matrix corresponding to  $\mathbf{W}$  is obtained from (3) and (2). The first partial derivative is similar to (9):

$$\frac{\partial \ell}{\partial W_{ik}} = \sum_{j=1}^m \sigma_j^{-2} \left\{ -\nu_{ij} + r_{ij} \frac{\mathbb{I}_1\left(\frac{r_{ij}\nu_{ij}}{\sigma_j^2}\right)}{\mathbb{I}_0\left(\frac{r_{ij}\nu_{ij}}{\sigma_j^2}\right)} \right\} \frac{\partial \nu_{ij}}{\partial W_{ik}},$$

while the second partial derivative is

$$\frac{\partial^2 \ell}{\partial W_{ik'} \partial W_{ik}} = \sum_{j=1}^m \sigma_j^{-2} \left\{ -\nu_{ij} + r_{ij} \frac{\mathbb{I}_1\left(\frac{r_{ij}\nu_{ij}}{\sigma_j^2}\right)}{\mathbb{I}_0\left(\frac{r_{ij}\nu_{ij}}{\sigma_j^2}\right)} \right\} \frac{\partial^2 \nu_{ij}}{\partial W_{ik'} \partial W_{ik}} + \sum_{j=1}^m \left\{ -\frac{1}{\sigma_j^2} + \frac{r_{ij}^2}{\sigma_j^4} h\left(\frac{r_{ij}\nu_{ij}}{\sigma_j^2}\right) \right\} \frac{\partial \nu_{ij}}{\partial W_{ik}} \frac{\partial \nu_{ij}}{\partial W_{ik'}}.$$

$\widehat{\mathbf{H}}$  is equal to the negative second derivative w.r.t.  $W_{ik}$  over  $i$  and  $k$ , and  $\mathbb{I}_s(x)$  is the modified Bessel function of the first kind of order  $s$ . Note that, any order of derivative of  $\ell_i$  w.r.t.  $W_{i'k}$  is 0 if  $i \neq i'$ , making  $\widehat{\mathbf{H}}$  block diagonal, and

$$h(x) := \frac{d}{dx} (A_1(x)) = \frac{1}{2} \left[ \frac{\mathbb{I}_0(x) \{\mathbb{I}_0(x) + \mathbb{I}_2(x)\} - 2\mathbb{I}_1^2(x)}{\mathbb{I}_0^2(x)} \right] \quad (\text{S7})$$

The part of the penalized likelihood from the Rice density contributes to  $\widehat{\mathbf{H}}$ , and the Hessian of the penalty part contributes to  $\mathbf{\Lambda} \otimes \mathbf{\Psi}^{-1}$ , producing the  $\widehat{\mathbf{\Omega}}$  matrix.

## S2. SUPPLEMENT TO SECTION III

### A. The trajectory of the objective function in (4) when using OSL-EM and AECM

Figure S1 shows the path of the objective function in (4) for the example in Section III-A2a. We see that the penalized log-likelihood for OSL-EM does not always increase in every iteration. In fact, in this example, it oscillates, especially with increased desired precision in terms of relative error. However, the penalized log-likelihood increases for AECM, as is guaranteed by theory. Further, with the increasing ascent property, the algorithm usually converges with fewer iterations than OSL-EM.

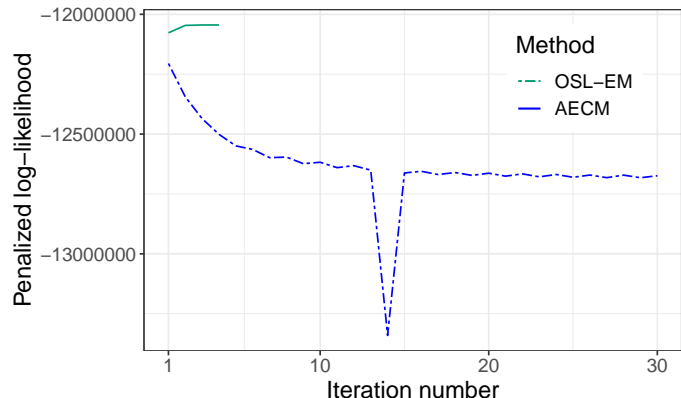


Fig. S1. The path of the objective function in (4), using OSL-EM and AECM.

### B. Bootstrap validation of SE calculations

We validate our theoretically derived approximate SEs using the parametric bootstrap. Our bootstrap procedure was as follows. First, using the estimated  $\widehat{\mathbf{W}}$ , we obtained resampled training images were generated using the equations (1) and (2) with the train TE and TR settings. For the  $b$ th resampled training images, we used AECM to have estimated  $\widehat{\mathbf{W}}_b^*$ ,  $b = 1, 2, \dots, B$ , with  $B$  as the number of bootstrap replications, and inserted them, along with the test (TE, TR) (1) used to get  $\widehat{\nu}_b$  for these settings. From these resampled synthetic images, the standad deviations of  $c'\widehat{\nu}_b$ , over  $b = 1, 2, \dots, B$ , can be calculated to provide us with estimated SEs of  $c'\widehat{\nu}$  which can be compared to our theoretically derived approximate SEs. However, we note that our validator has sampling variability. In order to account for this variability, we calculated the standard deviations of these bootstrap SEs. We used a jackknife-type estimator to estimate this SD. Specifically, from the bootstrap replications, we used a leave-one-out method to get  $B$  leave-one-out bootstrapped SE estimates. The standard deviation over these  $B$  leave-one-out SE estimates can be used to obtain a SE of the bootstrap-estimated SE. Our experiments indicate that the theoretical SEs of the ROI means of the synthetic images are within one SE of the bootstrap-estimated SEs and so are not significantly different.

### C. Consistency of Estimates and predictions

Figure S2 shows the performance of LS and AECM against average SNR. While Figure S3 shows the prediction performances of the two procedures vis-a-vis average SNR. It shows that the penalized method always provides better estimates of  $W_1$  and  $W_2$ . Although, LS appears to provide better estimates of  $W_3$  than at unrealistically high SNR settings, the difference in the errors is practically negligible. This is also reflected by the uniformly better prediction accuracy of the penalized method. Also, the estimation and prediction error decreases faster with increasing SNR under AECM than LS.

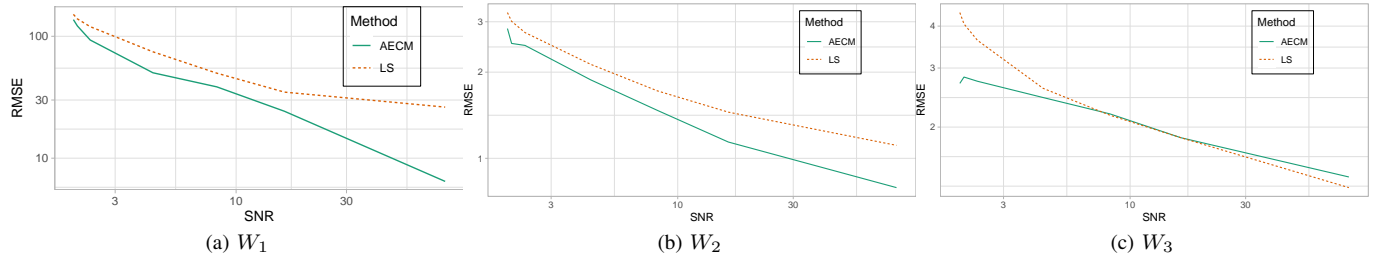


Fig. S2. The errors in estimating  $W_1, W_2, W_3$  vs average SNR; Both axes are in log-scale.

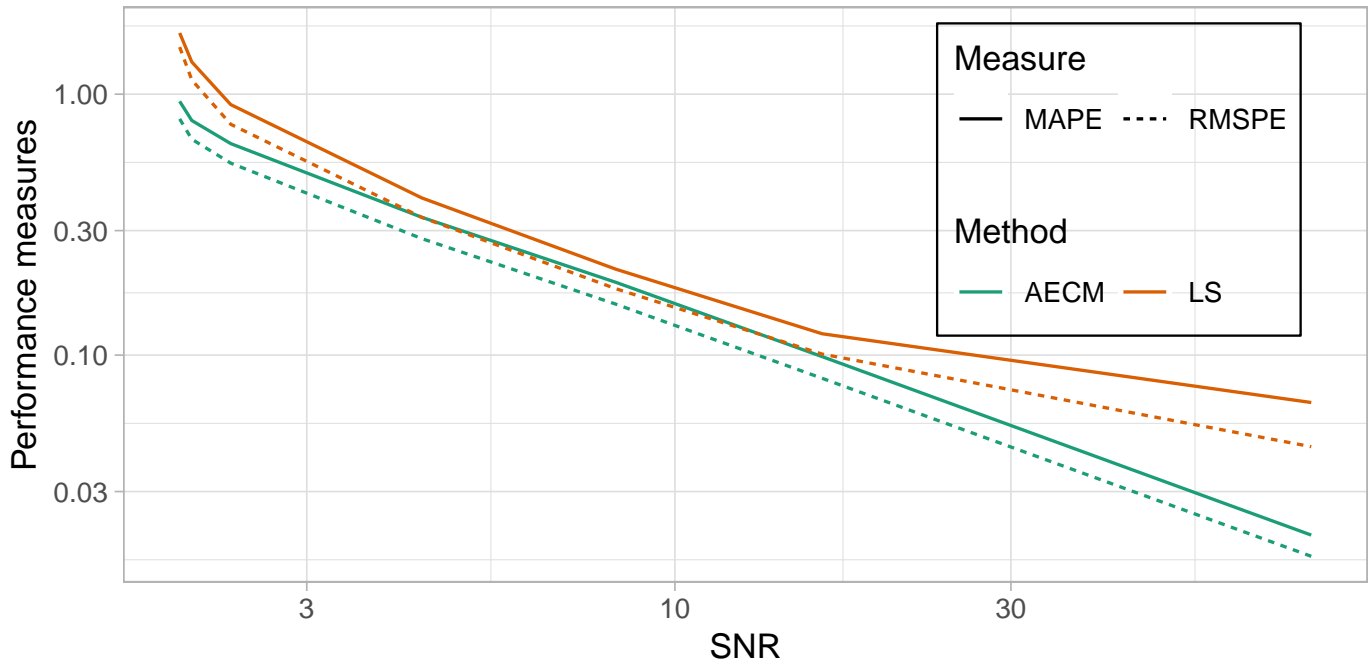


Fig. S3. Performance measures from the Brainweb data vs different noise intensity